APPENDIX A

"Emission and Applications of Uncertainty in methane Emissions Quantification Technologies: A Bayesian Approach."

This is a draft of a journal manuscript that defines the empirical uncertainty quantification technique described in Sec. 5.2.

Estimation and Applications of Uncertainty in Methane Emissions Quantification Technologies: A Bayesian Approach

Augustine Wigle[a,*], Audrey Béliveau[a], Daniel Blackmore[b], Paule Lapeyre[b], Kirk Osaditz[c], Christiane Lemieux[a], Kyle J. Daun[b]

[a]*Department of Statistics and Actuarial Science, University of Waterloo, Waterloo, Canada*
[b]*Department of Mechanical and Mechatronics Engineering, University of Waterloo, Waterloo, Canada*
[c]*Carbon Management Canada, Calgary, Alberta*

Abstract

An accurate understanding of uncertainty is needed to properly interpret methane emission estimates from the upstream oil and gas sector in a variety of contexts, from component-level measurements to yearly industry-wide inventories. One possibility is to derive an uncertainty estimate from the physical model that connects the measurement data to the emission estimates directly, but this information is often proprietary and thus unavailable to end users. Instead, we provide a method to develop probability distributions of measurements given a true emission rate empirically using controlled release data. This method is completely technology-agnostic, and provides a route to summarise uncertainty without the need to release proprietary modelling or data. To demonstrate the wide applicability of the method, we introduce an algorithm that can be used to synthesize the uncertainty model and measurement-based surveys to produce an uncertainty range for new measurements in the field.

Keywords: methane, uncertainty quantification

1. Introduction

Deep and rapid reductions in methane emissions from leading anthropogenic sources, especially upstream oil and gas activities, are crucial in order to avoid the worst outcomes of climate change [1], but doing this requires instrumentation that can reliably detect and quantify these emissions. Technologies for doing this include: quantitative optical gas imaging (QOGI) using mid-wavelength infrared (MWIR) cameras [2, 3, 4]; stationary [5] and mobile [6, 7, 8] methane

*Corresponding author
Email address: amhwigle@uwaterloo.ca (Augustine Wigle)

concentration sensors; and airborne [9, 10] and satellite-based [11] measurements. All of these systems utilize a measurement model that relates direct observations and auxiliary inputs to the methane emission rate. Often the measurement model consists of a spectroscopic sub-model that connects some radiometric measurement to a column density (ppm$\times$m) or path-averaged concentration estimate (ppm), and an advection sub-model, usually informed using anemometry data. The output of the inversion procedure is typically a point estimate of the methane emission rate from the source (e.g., kg/hr).

Emissions estimates can only be interpreted properly in the context of uncertainty. This aspect is particularly important in view of existing and emerging methane emissions regulations and reduction commitments [1, 12, 13], e.g., to answer the question "with what probability is this facility compliant with a particular regulation?" Methane leak detection and repair (LDAR) programs should also be optimized with quantification uncertainty in mind to give the best trade-off between cost and emissions reductions, as it has been shown that high quantification uncertainty contributes to certain types of LDAR programs being less cost effective [14]. Further, methane emissions measurements are used to develop broader jurisdiction-wide and global inventories [15, 16, 9], which are needed to assess progress towards emissions reduction targets and to inform policies and regulations, but these decisions can only be made in the context of uncertainty. Therefore, there is a need for transparent techniques for estimating emissions uncertainty that can be applied consistently in different contexts.

Approaches for quantifying methane emission uncertainty may be categorized as either physics-based or data-driven. Physics-based approaches address uncertainty associated with measurement noise, uncertain model inputs, and, especially, the model errors induced by the approximations and simplifications needed to derive a tractable measurement model, in an explicit way. As an example, Montazeri et al. [17] derive formulas for different error components of QOGI estimates, with the aid of virtual data generated from a computational-fluid dynamics large eddy simulation (CFD-LES). Caultron et al. [8] developed uncertainties for emission estimates obtained from a truck-mounted concentration sensor and inverse Gaussian plume model by accounting for uncertainty in the Gaussian model diffusion coefficient, emission source and height, and wind speed and stability class. Cambaliza et al. [18] developed uncertainties for emission estimates inferred from aircraft-based concentration measurements using different values for the background carbon dioxide and methane, depth, changes in the convective boundary layer height, and perpendicular wind speed parameters.

While physics-based approaches provide key insights into the uncertainty of methane emission estimates obtained from various technologies, and how they should be deployed to minimize these uncertainties, they also have several key drawbacks. First, they require detailed knowledge of the measurement model, which may be very complex or unavailable due to proprietary aspects of the technology. Second, the results of a physics-based uncertainty analysis are specific to a given technology and will not be broadly applicable, requiring cumbersome effort for every technology of interest. Third, results of a purely

physics-based uncertainty estimate may not agree with what is observed in real-world scenarios due to missing or inadequate modelling of uncertainty sources. Moreover, existing physics-based uncertainty analyses do not include methods or procedures for how the results should be applied in practice, and there is a lack of consistency in reporting of the results [8]. For example, most physics-based approaches do not show how their results should be used to derive a 95% confidence interval based on a given measurement from the technology.

Empirical approaches to uncertainty quantification rely on a statistical model which compares true and measured emission rates from controlled-release data. The statistical model can then be used to predict future measurements given a true emission rate, or inverted to give a confidence interval for the true emission rate given a measurement. Empirical approaches have two key benefits over physics-driven approaches: 1) they are data-driven, meaning the results will likely resemble what is actually observed in the field, and 2) the statistical framework can be leveraged to provide unified and consistent guidelines for how the results of the uncertainty analysis should be used in practice.

Empirical approaches require data from controlled-release field trials. To this end, many single-blinded or double-blinded field trials have been conducted with the goal of assessing the performance of methane emissions quantification technology, e.g., [19, 20, 21, 10, 22]. However, empirical approaches employed on these data have mainly been limited to simple linear regression approaches which do not allow for quantification uncertainty to vary with the emission rates [19, 20, 21, 10], with the exception of [22], who provide an approach to derive the distribution of the true emission rate given a measurement from an airborne methane detection and quantification technology.

In this work, we introduce a flexible empirical framework to elucidate quantification uncertainty that can be applied to any technology modality and illustrate its use using field trial data from two campaigns carried out using four methane detection and quantification technologies as well as controlled release data reported by [22]. The empirical framework allows for the derivation of two important probability distributions: 1) the distribution of measurements given the true emission rate and 2) the distribution of the true emission rate given a measurement. The first distribution is a building block to the second distribution, and has the potential to be incorporated into simulation software that models LDAR programs such as FEAST, LDAR-Sim, and AROFemp [23, 24, 25]. The second distribution is an important input to simulation methods used to derive measurement-based inventory estimates such as [26]. Our approach to deriving the second distribution also provides the opportunity to incorporate context-specific information into the analysis, such as knowledge of the emission rate distribution in a given region. The results of the analysis are data-driven and the design of the field trials allows for the assessment of the potential real-world effectiveness of the uncertainty quantification results.

Figure 1: Technologies studied in the field trials. Top row, left to right: QOGI A, QOGI B, QOGI C. Bottom row, left to right: airborne NIR HSI, truck-based TDLAS.

2. Materials and Methods

2.1. Methane Quantification Technologies

We demonstrate the analysis procedure using controlled release data from four methane quantification technologies, three of which were evaluated in the field trials described in Sec. 2.2: QOGI; truck-mounted tunable diode laser-absorption spectroscopy (TDLAS); and airborne near-infrared hyperspectral (NIR HS) imaging. We also consider an airborne TDLAS system ("Gas Mapping LiDAR™ " (GML) from Bridger Photonics, Inc.) based on data reported in Conrad et al. [22]. Examples of the technologies investigated in the field trials are shown in figure 1.

2.1.1. Quantitative Optical Gas Imaging (QOGI)

QOGI systems are almost exclusively based on a mid-wavelength infrared (MWIR) camera that contains a cold filter centered on the 3.34 μm methane vibrational-rotational band. The intensity entering the camera aperture is imaged through the cold-filter and onto a focal plane array (FPA) that produces a pixel intensity. The cameras are usually calibrated to generate a spectrally-averaged absolute intensity along each pixel line-of-sight. The camera data is then analyzed in near real-time by software on a peripheral tablet. The measurement model is composed of a spectroscopic sub-model that generates a column density map of the gas, and an advection model that infers a 2D projected velocity field from the apparent plume motion between successive images. These quantities are then combined to obtain a mass flow rate (e.g, kg/s).

The reliability of QOGI-derived emission estimates depends on factors that include measurement distance between the plume and the camera, thermal

contrast between the plume and the background, wind speed, and leak rate [27, 19, 28]. Identifying favorable measurement scenarios draws considerably on operator experience [29]. Three QOGI systems were deployed by three operators of varying experience, as summarized in Table 1.

Table 1: QOGI operators and equipment

Operator	**Experience**	**System**	**Field Trial**
A	Professional	FLIR GF320 with Providence QL320 (v. 3.0.0.5)	1
B	Professional, new to system	OPGAL EyeCGas (v. 1.0.24)	2
C	Novice	FLIR GFx320 with FLIR QL320 (v. 1.4.1)	1 & 2

QOGI Operator A used a FLIR GF320™ camera with a Providence QL320™ tablet (v. 3.0.0.5); QOGI Operator B used the OPGAL EyeCGas™ (v. 1.0.24) and QOGI Operator C used a FLIR GFx320™ camera with the FLIR QL320™ Tablet (v. 1.4.1). Notably, while Operator B was an experienced QOGI operator, they were unfamiliar with the OPGAL system during the field trial. QOGI Operator A was highly experienced and familiar with their equipment, while QOGI Operator C was a novice, having less than six months of experience with the system.

2.1.2. Truck-mounted TDLAS

Methane releases were also quantified using a truck-mounted TDLAS system (Boreal Laser GasFinder 3 VB™). The absorptance, and therefore methane column density (e.g., ppm·m), is inferred through wavelength-modulation spectroscopy (WMS) [30] and then converted to a path-average concentration (ppm). The truck traversed the plume at distances ranging from 50 to 100 m downwind of the release point. Methane concentrations were measured at one second intervals; these concentrations and wind speeds obtained from an ultrasonic anemometer operated by the service provider were then processed using a backwards Lagrangian stochastic quantification algorithm [31, 32] to obtain a release estimate for each plume transect.

2.1.3. Airborne NIR HS imaging (GHGSat-AV™)

The airborne NIR HS system (GHGSat-AV™) consists of a downward-looking wide-angle Fabry-Perot imaging Fourier transform spectrometer that operates between 1630-1655 nm [33], mounted inside an aircraft [34]. The aircraft overflew the releases at an approximate altitude of 250 m above ground level and airspeed of 240 km/hr. Thermal emission from the gas and ground is negligible over this wavelength range; instead, the camera images sunlight transmitted through the atmosphere, reflected from the ground, and transmitted back to the camera. The methane column density is inferred from the attenuation of the transmitted light via a multi-layer spectroscopic model, and then combined

with an advection model [35] using wind data from an online weather model to find the emission rate.

2.1.4. Airborne TDLAS

Bridger's airborne GML™ system consists of two tunable diode lasers, and a sensor that detects the ground-reflected laser light. One laser is used for range finding and determining ground reflectivity, while the other scans the 1651 nm CH_4 absorption line to determine column density. The lasers move in a conical pattern, which forms an ellipsoidal swath on the ground. Reflected light from the range-finding and methane-absorbing lasers are combined to form a column density via WMS. The column density estimates across the swath are used to form a 3D plume concentration map, which is combined with an advection model using wind speed from online weather data to obtain a release rate [20].

2.2. Field Trial Design and Execution

The QOGI, truck-mounted TDLAS, and airborne NIR HS imaging systems were evaluated through two controlled release field campaigns executed at Carbon Management Canada (CMC)'s Newall County Research Station near Brooks, Alberta, the first during April 20-26 2022 and the second during September 25-October 1, 2022. Technology developers and service providers were invited to attend the field trials and quantify emissions of natural gas in a variety of industrially relevant scenarios, including 1.7 m, 3.4 m, and 4.8 tall stacks, and a 14-m tall unlit flare, following their standards-of-practice.

An assay showed that the natural gas consisted of 94.2 % methane, 3.4 % ethane, 1.1 % propane, and 1.3 % minor components, predominantly N_2 and O_2 in roughly atmospheric abundances. The gas was released from a compressed cylinder via a regulator valve and flowed through a heat exchanger to condition the gas to atmospheric temperature. The conditioned gas then passed through a mass flow controller (Alicat MCR-2000SLPM - D-PAR) and discharged to the atmosphere in a manner that depended on the release scenario as shown in figure 2.

Local meteorological conditions were measured using a portable 81000-L RM Young 3D ultrasonic anemometer and a Davis WeatherLink Pro+™ weather station. The portable anemometer was located 2.25 m above the ground. Background measurements of methane and other relevant species were monitored throughout the tests using a Picarro cavity ringdown spectrometer located in a structure approximately 250 m from the release locations. Background methane measurements were between 2 to 2.5 ppm throughout the tests. Meteorology and controlled release data for these field trials are provided in the supplemental information (SI).

Service providers did not have access to meteorology data; instead, they conducted their own on-site measurements or relied on third-party weather models, as they would when deploying the technology in a practical scenario. Service providers then compiled their own estimates and provided them to the academic team.

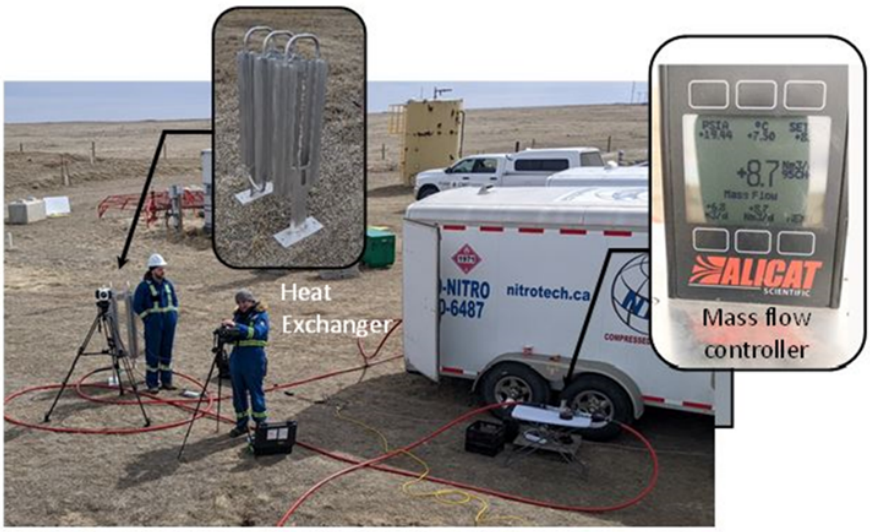

Figure 2: Controlled release set-up including heat exchanger and mass flow controller.

Additional data was taken from controlled release studies reported in the literature: Bridger GML system was taken from the controlled, fully-blinded release study reported by Conrad, et al. [22].

Table 2: Summary of technologies, providers, and available data from the field trials and external sources. N_1 and N_2 refer to the number of observations collected for a given technology during the first field trial and second field trial, respectively."Other" refers to data from Ref. [22].

Technology	N_1	N_2	Other
QOGI Operator A	117	0	NA
QOGI Operator B	0	71	NA
QOGI Operator C	14	106	NA
Truck TDLAS	142	125	NA
Aerial TDLAS	NA	NA	405
Aerial NIR HSI	46	37	NA

3. Uncertainty Quantification

3.1. Models for Uncertainty Using Controlled Release Data

We propose a statistical model that answers the following question: For a given true emission rate, what range of measurements could be expected, given the observed controlled release data, in the context of model error and measurement noise? We take a Bayesian approach to fitting the model and thus in Sec. 3.1.2 we give a brief overview of Bayesian analysis, followed by technical details

that include the prior distributions, Sec. 3.1.3, and model selection methods, Sec. 3.1.4.

3.1.1. Novel Flexible Model

Let Q_i be the true emission rate corresponding to the ith observation in the field trial, and M_i be the emission rate estimated by the technology for the ith observation, $i = 1, \ldots, n$ where n is the total number of observations for the given technology. The relationship between Q_i and the bias and variability of M_i can be complicated, since both the bias and the variability may change over the range of Q_i. Additionally, the relationship between Q_i and M_i may not be strictly linear, as shown in e.g. figure 3. The model must also account for the fact that all technologies may report a "false positive", that is, estimating a non-zero M_i when $Q_i = 0$.

A flexible likelihood which allows the bias and variance of M_i to vary with Q_i and incorporates the possibility of false positives is given by

$$\log(M_i) = \log(\phi_i) + \epsilon_i, \tag{1}$$

where

$$\epsilon_i \sim \mathrm{N}(0, \sigma_i^2)$$

and

$$\phi_i = \mathrm{median}(M_i).$$

A specification for ϕ_i is

$$\phi_i = \begin{cases} \alpha_0 + \alpha_1 Q_i + \alpha_2 Q_i^2 & Q_i \leq \gamma; \\ \alpha_0 + \beta_0 + (\alpha_1 + \beta_1) Q_i & Q_i > \gamma. \end{cases}$$

To ensure that the function is continuous at $Q_i = \gamma$, we impose the restriction that $\beta_0 = \alpha_2 \gamma^2 - \beta_1 \gamma$. In this likelihood, there is a quadratic relationship between ϕ_i and Q_i for values of Q_i smaller than a threshold γ and a linear relationship for larger values of Q_i. This likelihood is normal on the log scale, which corresponds to a log-normal likelihood on the measurement scale.

The specification of ϕ_i can be modified to give the best prediction results and fit to the data. For example, the threshold parameter γ, β_0 and β_1 could be removed, which would give a quadratic relationship over the whole range of Q_i. Table 3 summarizes the parameters that may be removed and Section 3.1.4 shows how the likelihood is chosen.

The model can be rewritten to facilitate interpretation by exponentiating both sides of Eq. (1):

$$M_i = (\phi_i) \times e^{\epsilon_i}, \tag{2}$$

where ϕ_i is the median measurement for a true emission rate of Q_i.

The likelihood in Eq.(1) is an extension of the scheme proposed by Conrad et al. [22]. That is, their model is a special case of our likelihood where $\alpha_0 = 0$, $\alpha_2 = 0$, $\beta_0 = 0$, $\beta_1 = 0$, and $\sigma_i^2 = \sigma^2$ for all $i = 1, \ldots, n$. Briefly, they assume the median value of M_i has a multiplicative relationship with Q_i, that is,

$\phi_i = \alpha_1 \times Q_i$, and the multiplicative error term has a constant variance over the range of Q_i. Our model expands on this in three ways. First, we allow for linear and quadratic relationships between the median measurement and Q_i rather than a strictly multiplicative one. This is useful in modelling more complex relationships. Additionally, it allows false positives to be modelled via α_0. Second, the inclusion of the threshold parameter t allows more flexibility in modelling the relationship between the median of M_i over the range of Q_i rather than assuming a common median function for all Q_i. Third, we investigate different variance structures for ϵ_i which can allow the variance to change with Q_i to more accurately model the patterns observed in controlled data from some instrumentation rather than assuming a constant variance. Another difference between this approach and that of [22] is that they investigate different distributions for the error term, whereas we restrict ourselves to the log-normal distribution, but investigate different forms for the median and variance which are motivated by the data. Finally, we take a fully Bayesian approach to estimation and inference discussed in section 3.1.2 whereas [22] uses a (frequentist) maximum likelihood approach.

It is important to note that in this model the errors are additive on the log scale, which implies multiplicative errors on the raw measurement scale as shown in Eq. (2). The simplest way to model the variation is to set the variance of ϵ_i to a constant, $\sigma_i^2 = \tau^{-1}$ for all i, where τ is referred to as the precision parameter. Multiplicative errors may be suitable for lower and moderately-sized emission rates, but for large values of Q_i purely multiplicative errors may overestimate variability for some technologies. A possible explanation for this is that for smaller emission rates, both the error in raw concentration or column density estimates and error in the advection model are significant, leading to product uncertainty. For larger emission rates, however, either raw measurement error or advection model error dominates, leading to sub-multiplicative errors in this range. To accommodate this, we also propose using $\sigma_i^2 = (\tau + Q_i/\eta)^{-1}$ as an alternative variance structure for ϵ_i which allows the variability of the error terms to decrease with increasing Q_i. The approach to choosing an appropriate likelihood, including the variance specification, is described in Sec. 3.1.4.

This section concludes with interpretations of the parameters in the likelihood. Threshold parameter γ allows the linear relationship to change for larger values of Q_i. α_0 represents the median measurement when the true emission rate is zero, which accounts for false positives. Parameters α_1 and α_2 are the coefficients for Q_i and Q_i^2, describing the quadratic relationship between the median measurement and the true emission rate when the true emission rate is less than the threshold. Sums $\alpha_0 + \beta_0$ and $\alpha_1 + \beta_1$ are the slope and intercept of the linear relationship between the median measurement and Q_i when Q_i exceeds the threshold. Some technologies exhibit simpler relationships between Q_i and the median of M_i, in which case some or all of γ, α_2, β_0, and β_1 may be dropped from the model. Finally, two different variance specifications were used in the likelihood: either $\sigma_i^2 = \tau^{-1}$ or $\sigma_i^2 = (\tau + Q_i/\eta)^{-1}$. In the former case, τ^{-1} is the variance of all measurements on the log scale. In the latter specification, τ^{-1} is the variance of the measurements when $Q_i = 0$ and c controls how

much the variance changes as Q_i increases from zero. A larger value of η corresponds to a milder reduction in variance as Q_i increases. Table 3 summarizes the parameters in the likelihood, their units, and scenarios in which they may be included or removed.

3.1.2. Bayesian Analysis

The model parameters are estimated using a Bayesian approach. This is done for several reasons: (i) the method is flexible, allowing the likelihood to be tailored to the data; (ii) data can be synthesized seamlessly from multiple sources (e.g., multiple measurement campaigns or different measurement modalities); (iii) it explicates the use of prior information; and (iv) it provides the full probability distribution of measurements given a true emission rate, amounting to a comprehensive definition of what is known about the emission rate (see Sec. 4.2).

Let the unknown parameters of a statistical model for the measurement M_i given a fixed true emission rate Q_i be represented by vector $\underline{\theta}$. In the Bayesian framework, these parameters are envisioned as random variables defined by probability distributions that are related by Bayes' equation,

$$p(\underline{\theta} \mid \underline{M}) = \frac{p(\underline{M} \mid \underline{\theta})p(\underline{\theta})}{p(\underline{M})}, \tag{3}$$

where $\underline{M} = (M_1, M_2, \ldots, M_n)'$. The probability distribution of interest is the *posterior* distribution, $p(\underline{\theta} \mid \underline{M})$, which summarises the information about $\underline{\theta}$ in the observed measurements along with any external or "prior" knowledge we may have about $\underline{\theta}$. The likelihood distribution, $p(\underline{M} \mid \underline{\theta})$, is the probability distribution of the set of measurements for a fixed value of $\underline{\theta}$ and is also a function of the true emission rates $\underline{Q}$, which is fixed and thus suppressed in the notation in Eq. (3). It describes how likely it is to observe $\underline{M}$ for a given value of $\underline{\theta}$ and $\underline{Q}$ in the context of measurement noise and model error. Under the assumption that measurement errors are independent between measurements, we also have that $p(\underline{M} \mid \underline{\theta}) = \prod_{i=1}^{n} p(M_i \mid \underline{\theta})$. The prior distribution, $p(\underline{\theta})$, describes what is known about the unknown parameters before data is collected. Prior distributions for the proposed models are discussed in Sec. 3.1.3. Finally, $p(\underline{M})$ is the marginal distribution of the data, which is constant for fixed data.

The posterior $p(\underline{\theta} \mid \underline{M})$ is estimated using Markov Chain Monte Carlo (MCMC) sampling, which generates a set of samples from the posterior distribution of $\underline{\theta}$ [36]. These samples are readily used to derive quantities of interest, such as credibility intervals. MCMC sampling is done using Just Another Gibbs Sampler (JAGS)[37] via the runjags R package [38].

We wish to understand the distribution of a measurement given a fixed value of Q_i. Let $\tilde{M}_i$ represent a new, unobserved measurement and Q_i be an accompanying true emission rate. Then we wish to find the posterior predictive distribution of $\tilde{M}_i$, given by $p(\tilde{M}_i \mid \underline{M}, Q_i) = \int p(\tilde{M}_i \mid \underline{\theta}, Q_i)p(\underline{\theta} \mid \underline{M})d\underline{\theta}$, which is the integral over $\underline{\theta}$ of the likelihood of M_i given fixed $\underline{\theta}$ and Q_i times the posterior distribution of $\underline{\theta}$. This distribution can be obtained via simulation using samples from the posterior.

3.1.3. Prior Distributions

As with any Bayesian model, an appropriate prior distribution depends on the context of the problem at hand, including pre-existing knowledge and the scale of the data. We summarise the units of each parameter in Table 3.

Parameter	Units	Exclusion criteria
α_0	$[M_i]$	*
α_1	Unitless	None
α_2	$[M_i]^{-1}$	†
β_0	$[M_i]$	*,†
β_1	Unitless	†
γ	$[M_i]$	†
τ	Unitless	None
η	$[M_i]$	†

Table 3: Summary of the units for each parameter in the likelihood, important to keep in mind when specifying prior distributions. Exclusion criteria: * = may be removed if technology does not have false positives in controlled release data, † = may be removed if its removal leads to a simpler model which has adequate fit and predictive performance.

The parameters of the likelihood to be estimated are α_0, α_1, τ, along with optional parameters α_2, γ, β_1, and/or η. All parameters are assumed to be independent, that is,

$$p(\theta) = p(\alpha_0, \alpha_1, \tau, \alpha_2, \gamma, \beta_1, \eta) = p(\alpha_0)p(\alpha_1)p(\tau)p(\alpha_2)p(\gamma)p(\beta_1)p(\eta), \qquad (4)$$

so we can specify individual prior distributions for each parameter.

We can derive empirical prior distributions by considering the role of each parameter in the model and their units. Since α_0 is the median measurement when the true emission rate is zero, it should be small and non-negative. It is parameterized by a gamma distribution, where the shape and rate parameters can be chosen so the mean of the distribution is similar to the mean false positives observed in the data. For example, for the data reported by QOGI Operator A, the average false positive is 0.27 kg/h so we use a gamma distribution with shape parameter = 0.5 and rate parameter = 2, which has a mean of 0.25 and variance of 0.125. Note that β_0 is a function of other parameters to ensure that the piece-wise function is C^1 continuous. A prior is not specified for this parameter.

In a simple linear model, α_1 is the slope of Q_i so for every one unit increase in Q_i, the median measurement increases by α_1 units. A perfect technology would have $\alpha_1 = 1$. Thus we use a prior for α_1 which has a median of 1 and is non-negative. Further, we seek a distribution with the property that for any constant $k > 1$, the probability that $\alpha_1 > k$ should be the same as the probability that $\alpha_1 < 1/k$, or in other words, the probability that the technology over-estimates by a factor of k is the same as the probability that it under-estimates by a factor of $1/k$. This property is desirable in the prior because information about under-

or over-estimation should only come from the data. Thus we use a standard log-normal distribution (shape parameter equal to one, location parameter equal to zero, and scale parameter equal to zero [39]) because it has this property. For example, if α_1 follows the standard log-normal distribution the probability that $\alpha_1 < 1/2 =$ probability that $\alpha_1 > 2 = 0.244$.

Coefficient α_2 is associated with Q_i^2 when $Q_i \leq \gamma$. Similarly to α_0 and α_1, we restrict this parameter to be non-negative to avoid taking the log of zero or a negative number. Due to the units of α_2, we use a prior with a relatively small variance. For example, if we wanted the variance to be equivalent to 10 kg/h, that equals 0.1 $[\text{kg/h}]^{-1}$. Thus we use a half-normal distribution with variance parameter equal to 1.

Parameter β_1 (unitless, nonnegative) represents the change in α_1 when $Q_i > \gamma$. As with α_1, we use a standard log-normal distribution as a prior for β_1.

The threshold parameter γ represents the value of Q_i for which the relationship with M_i changes from quadratic to linear. The parameter γ must be somewhere in the range of the Q_i data. We use a uniform prior distribution on (0, max) where max is determined by the largest value of Q_i observed in the data for a given technology.

Parameter τ represents either the inverse of the variance of measurements on the log scale in a constant variance model, or the inverse of the variance of measurements when $Q_i = 0$ on the log scale and is referred to as the precision parameter. We use a vague non-negative prior of a half-normal with variance parameter set to 100 on $\tau^{-1/2}$, as suggested in [40].

Finally, if the more complicated variance model is used, a prior must be chosen for η. Little external information is known about η except it must be non-negative. We use a half-normal with variance set to 100.

The sensitivity of results to prior specification was checked for all models. Results were obtained for the stated priors. Next, the model was refit with priors where the range and/or variance was changed for some parameters. The posterior distribution of each parameter was then compared between the two models. The resulting 90% prediction bands were also compared between the models. Unless otherwise stated in the results section, the model results were insensitive to the prior specification.

3.1.4. Model Selection

As discussed in Sec. 3.1.1, a variety of candidate models may be formed by adding or removing likelihood parameters, each of which may result in different implications for measurement bias and variability. For example, removing Q_i/η from the variance expression leads to a simpler model which has constant variance on the log scale. In general, a model with more parameters will fit the controlled release data better but may also be prone to over-fitting, which can result in poor predictive performance. Therefore, we use a combination of Deviance Information Criteria (DIC), prediction bands, and residual plots to select a model that provides a good trade-off between goodness of fit and complexity.

The Deviance Information Criterion, or DIC, combines goodness-of-fit to the training data and model complexity to provide an overall assessment of the

model [36]. It is analogous to the AIC, a frequentist model selection tool used by Conrad et al. [22] in the context of uncertainty modelling of methane quantification technologies. When comparing multiple models, a lower DIC value indicates a better balance between model fit and complexity, with differences of two or more considered meaningful [41].

We are also guided by plotting prediction bands derived from the posterior predictive distribution of measurements for different values of Q_i over a scatterplot of the data used to fit the model. If the prediction bands show a much wider or narrower spread than the data used to fit the model, this is an indication that the variance is not modelled well. Prediction bands can also be compared to additional data that was excluded from the model fit ("external data"), which indicates the generalizability of the model predictions. If the model predictions look similar to the external validation data, this is an encouraging sign that the model is suitable to be used under different conditions. Investigating the residuals, defined as the difference between the model-predicted value ($\hat{M}_i$) and the observed data point (M_i), that is, $\text{residual}_i = M_i - \hat{M}_i$ provides still more insight into areas of improvement for the model.

The DIC, prediction bands, and residual plots were used for model selection as follows: First, the simplest model possible with constant variance was fit to the data (a multiplicative model with α_1 if there are no false positives in the data or a linear model with α_0 and α_1 otherwise). The DIC was calculated using JAGS. Prediction bands were compared to the data used to fit the model and residual plots were inspected. If the prediction bands were much wider or narrower than the spread of the data, this indicated that the variance model should be explored. If the residual plots showed systematic problems, this indicated that the median specification should be explored. Models were then augmented as suggested by the diagnostic plots, refit, and DIC was re-calculated. This process was repeated until the diagnostic plots were satisfactory and the DIC was at least three less than that of the previous model.

4. Results and Discussion

4.1. Uncertainty Results

In this section, we present the selected likelihoods for five different methane quantification technologies/operators, discuss the performance, and comment on the generalizability of the model if applicable. The chosen models are summarized in Table 4.

4.1.1. QOGI Technologies

Prediction bands and posterior median predictions are shown for QOGI Operators A, B, and C in Figures 3, 4 and 5, respectively. All QOGI technologies underestimate emissions on average. The likelihoods from QOGI Operators B and C are best modelled using a quadratic function for the median below a small threshold, then a linear function. QOGI Operator A is best modelled using a quadratic function for the median. Data provided by Operator A has a more

Table 4: Summary of selected models for each methane quantification technology provider.

Technology	Selected likelihood	
	ϕ_i	σ_i^2
QOGI A	$\alpha_0 + \alpha_1 Q_i + \alpha_2 Q_i^2$	$(\tau + Q_i/\eta)^{-1}$
QOGI B	$\begin{cases} \alpha_0 + \alpha_1 Q_i + \alpha_2 Q_i^2 & Q_i \leq \gamma; \\ \alpha_0 + \beta_0 + (\alpha_1 + \beta_1) Q_i & Q_i > \gamma. \end{cases}$	τ^{-1}
QOGI C	$\begin{cases} \alpha_0 + \alpha_1 Q_i + \alpha_2 Q_i^2 & Q_i \leq \gamma; \\ \alpha_0 + \beta_0 + (\alpha_1 + \beta_1) Q_i & Q_i > \gamma. \end{cases}$	$(\tau + Q_i/\eta)^{-1}$
Truck TDLAS	$\alpha_0 + \alpha_1 Q_i$	$(\tau + Q_i/\eta)^{-1}$
Aerial TDLAS	$\alpha_1 Q_i$	$(\tau + Q_i/\eta)^{-1}$
Aerial NIR HSI	$\alpha_0 + \alpha_1 Q_i$	τ^{-1}

limited range than the other QOGI technologies - with a max Q_i value of 30 kg/h, compared to 80 kg/h for Operator C and 50 kg/h for Operator B. For QOGI technologies in general, the likelihood has more curvature in the lower range of Q_i while a linear relationship on the log scale is suitable for higher release rates.

The results for QOGI Operator B are quite distinct from those of Operators A and C. This may be attributed to this operator's lack of familiarity with the camera settings during the testing, as reported by the operator. This lack-of-familiarity manifests as an additional factor that influences (broadens and biases) the likelihood.

QOGI Operator C was present for both field trials. Only 14 measurements were made for this technology at the first field trial, which we use as external data. These data points fall within the 95% prediction band, suggesting that the model is generalizable.

4.1.2. TDLAS

Results from the selected models for truck and aerial TDLAS systems are shown in Figs. 6 and 7. The truck-based TDLAS tends to underestimate emissions, while the aerial technology overestimates on average.

For truck-based TDLAS, the model was fit using data from the second field trial, while data from the first field trial was used as external data to assess the model's generalizability. Most of the external data points fall within the prediction bands. However, the median trend appears different for the external data. A possible explanation for this is that weather conditions may have differed between trials one and two in such a way that estimates were systematically larger during the first trial than the second.

Figure 8 shows the predictions resulting from the Bayesian uncertainty model derived for the airborne TDLAS compared to the one presented by Conrad et al. [9]. The Bayesian model gives narrower prediction bands than the other model, which is particularly noticeable in the upper range of Q_i. This is likely due to the different variance specifications used in the models; the model in Ref. [22]

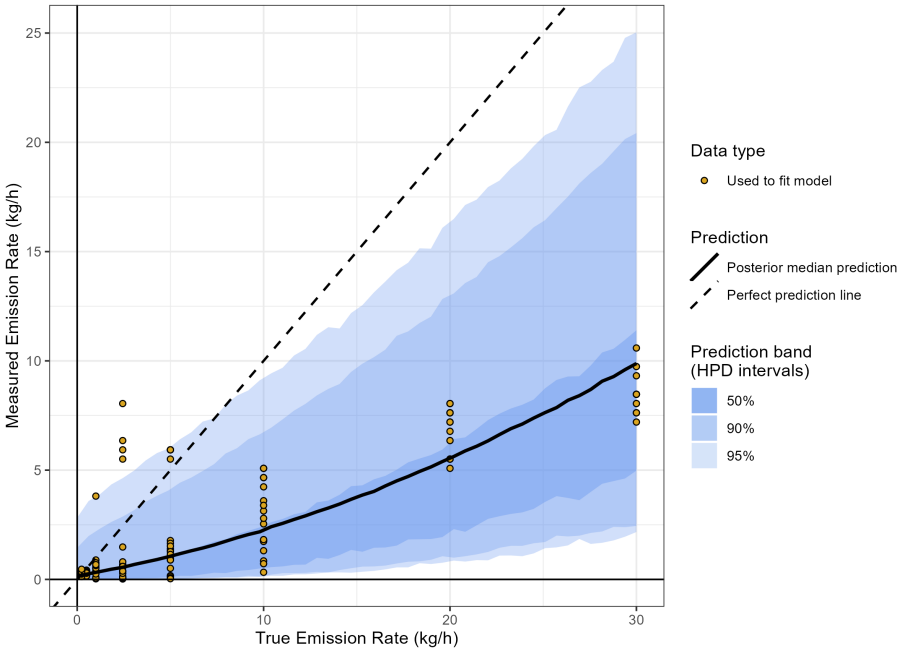

Figure 3: Uncertainty quantification model results for QOGI Operator A. The model was fit to data from the first field trial. No external data were available.

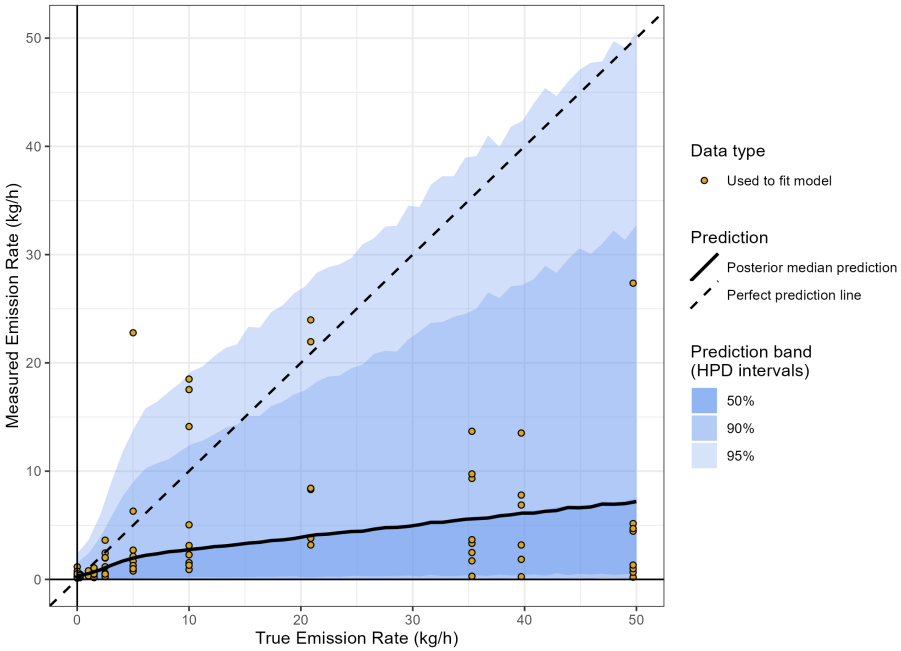

Figure 4: Uncertainty quantification model results for QOGI Operator B. The model was fit to data from the second field trial. No external data were available.

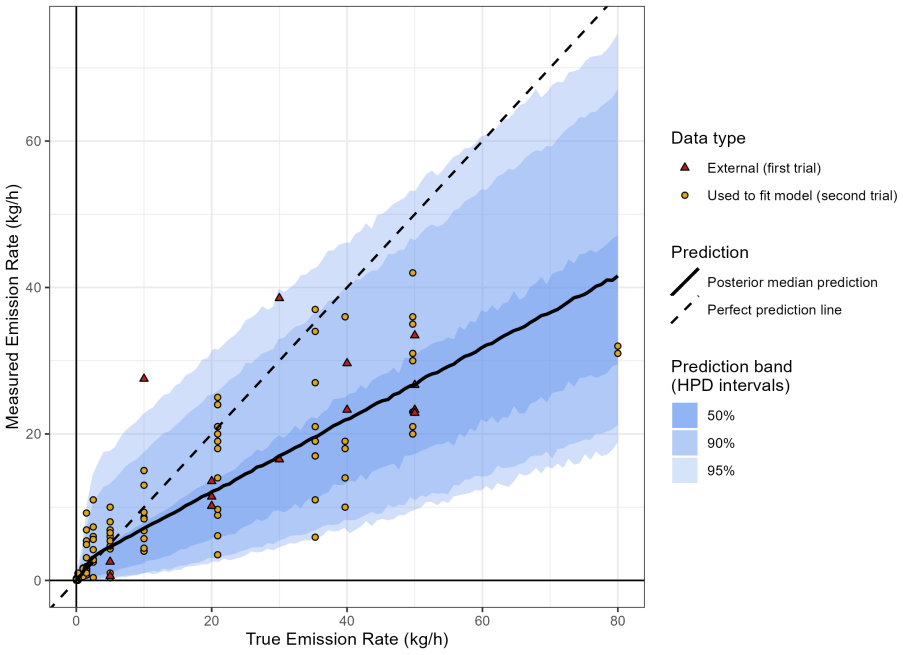

Figure 5: Uncertainty quantification model results from QOGI Operator C. The model was fit to data from the second field trial. Controlled release data from the first field trial was used as external data.

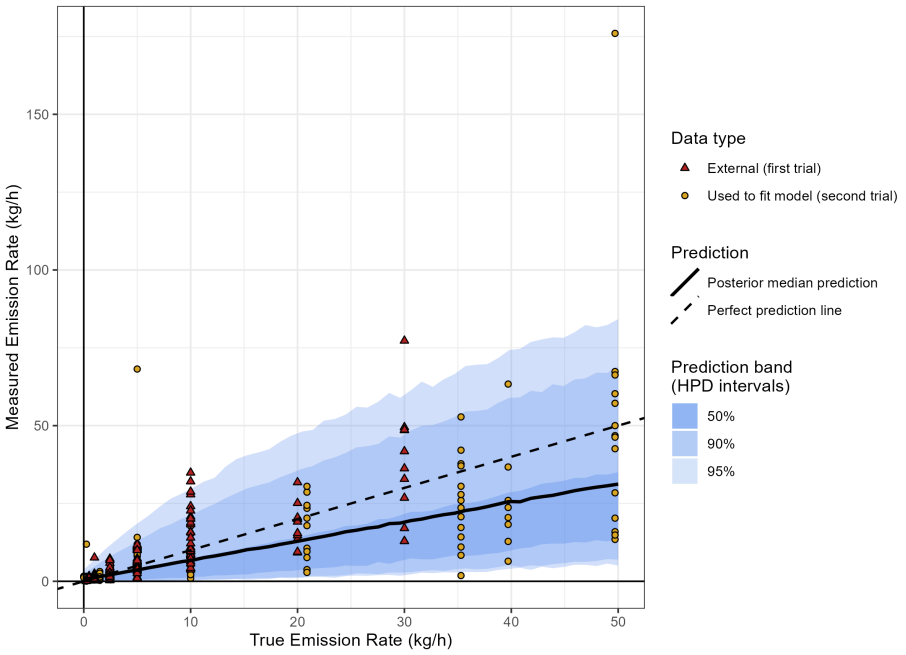

Figure 6: Uncertainty quantification model results for truck-based TDLAS data. The model was fit to data from the second field trial. Controlled release data from the first field trial was used as external data.

uses a constant variance whereas the selected model from our proposed Bayesian approach allows the variance to change with Q_i. The median predictions (solid black line) are very similar between the two models.

4.1.3. Airborne NIR HS Imaging

The prediction bands from the selected model for the airborne NIR HS imaging technology are shown in Fig. 9. The technology tends to overestimates emissions. The model was fit to data from the second field trial, while data from the first field trial were used as external data. There appear to be systemic differences between the data from the two field trials, with the data from the first field trial underestimating emissions more often, and data from the second field trial overestimating emissions more often. However, most of the external data points still fall within the 95% prediction bands, which is a positive indication of the applicability of the model. During the field trials, the operator remarked that the conditions were considered marginal due to excessive cloud cover and would not be typical of those under which commercial measurements were conducted, while those of the second field trial were nearly ideal. This could explain the lack of implausibly large estimates calculated during the first trial, as compared to the second field trial, where there two estimated measurements that

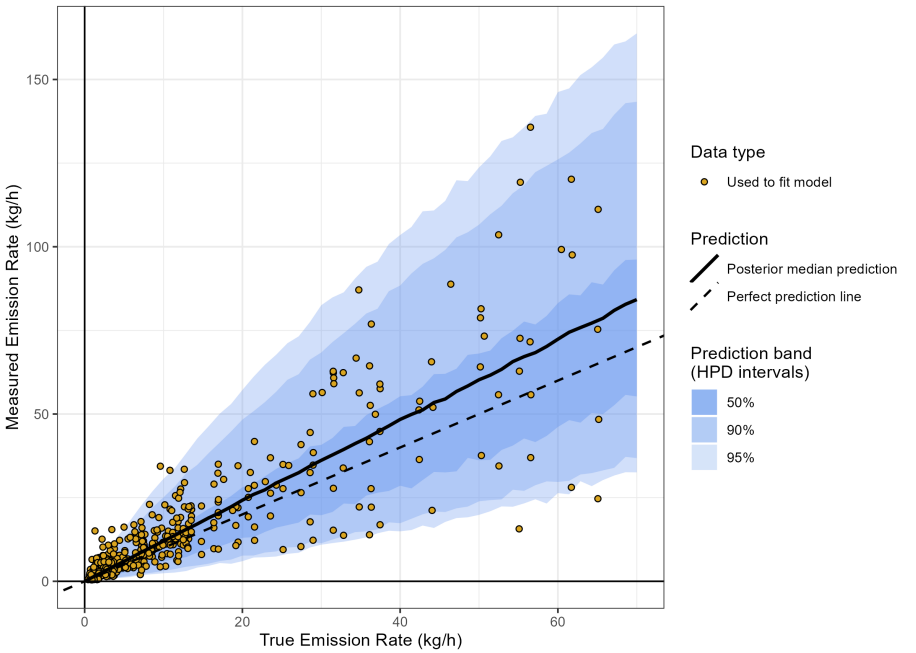

Figure 7: Uncertainty quantification model results for airborne TDLAS data provided by [22].

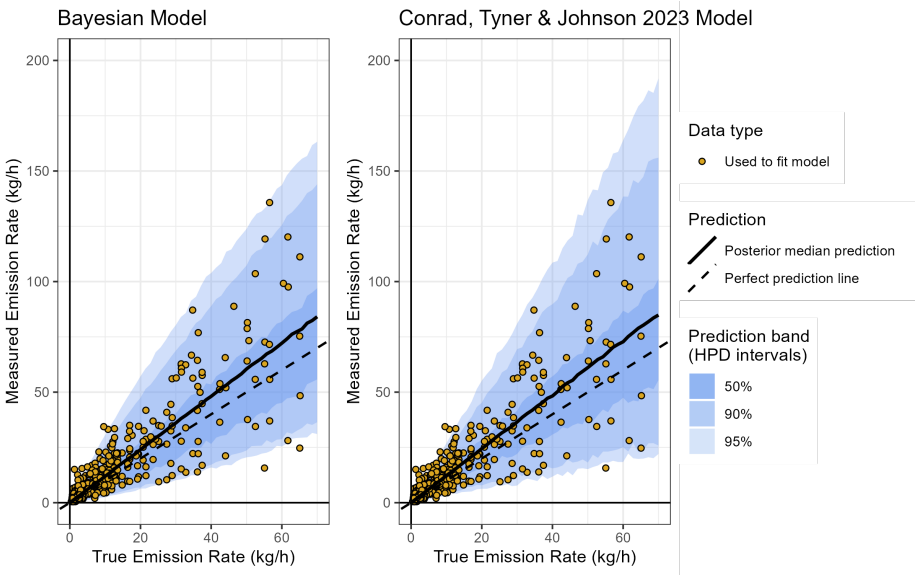

Figure 8: Side-by-side comparison of Bayesian model proposed in table 4 and that presented in [22] for airborne TDLAS.

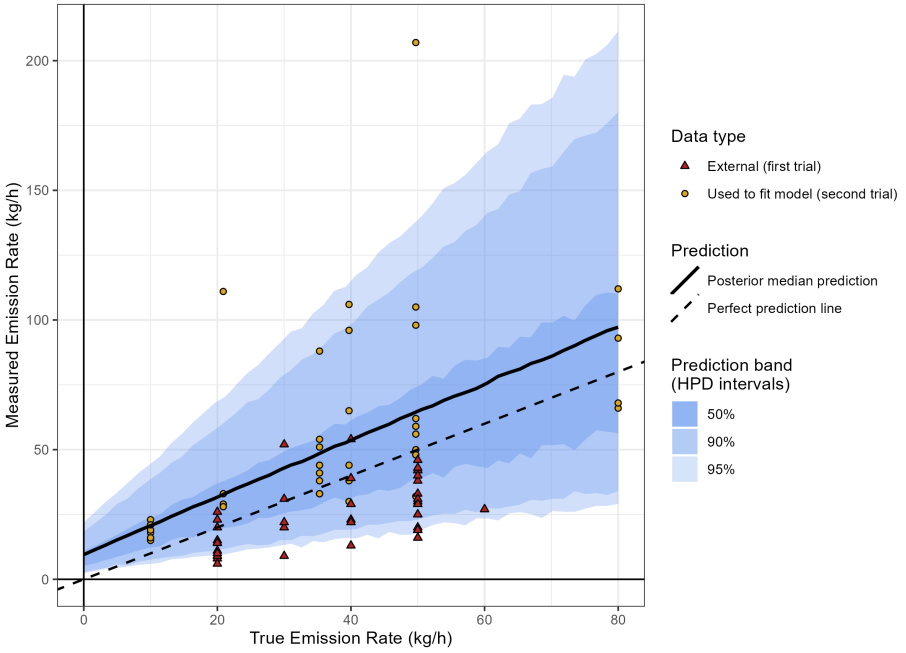

Figure 9: Uncertainty quantification model results for airborne NIR HS data. The model was fit to data from the second field trial. Controlled release data from the first field trial was used as external data.

are so large they fall outside the 95% prediction band.

4.2. Application: Quantifying Uncertainty in New Measurements

4.2.1. Algorithm

Finally, we describe a possible downstream application of the distributions derived in section 4.1. Suppose we wish to calculate a credible interval for the true emission rate based on methane measurements made in the field where the true emission rate is not known. Let Q^{new} represent the unknown true emission rate associated with the new measurement and M^{new} be the measurement made in the field. We wish to know the distribution of Q^{new} given M^{new} and our uncertainty model derived from controlled release data. The distribution of interest is $p(Q^{new} \mid M^{new}, \underline{M})$. Using Bayes equation, Eq. (3), we can say that

$$\begin{aligned} p(Q^{new} \mid M^{new}, \underline{M}) &\propto p(M^{new} \mid Q^{new}, \underline{M}) p(Q^{new} \mid \underline{M}) \\ &= p(M^{new} \mid Q^{new}, \underline{M}) p(Q^{new}), \end{aligned} \tag{5}$$

where the true emission rate is modeled as independent of the measurements from the controlled release trials. Computational techniques can be used to

obtain $p(M^{new} \mid Q^{new}, \underline{M})$. We can say that

$$p(M^{new} \mid Q^{new}, \underline{M}) = \int p(M^{new} \mid Q^{new}, \underline{\theta}, \underline{M}) p(\underline{\theta} \mid Q^{new}, \underline{M}) d\underline{\theta}$$
$$= \int p(M^{new} \mid Q^{new}, \underline{\theta}) p(\underline{\theta} \mid \underline{M}) d\underline{\theta}. \quad (6)$$

The distribution $p(M^{new} \mid Q^{new}, \underline{\theta})$ is the likelihood given by the uncertainty model from 3.1.1 where $Q_i = Q^{new}$. $p(\underline{\theta} \mid \underline{M})$ is the posterior distribution of $\underline{\theta}$ given the controlled release data. This integral can be approximated as follows:

1. Sample $\underline{\theta}^j$ $j = 1, \ldots, J$ times from $p(\underline{\theta} \mid \underline{M})$
2. For $j = 1, \ldots, J$, calculate $p(M^{new} \mid Q^{new}, \underline{\theta}^j)$
3. The integral in (6) $\approx \frac{\sum_{j=1}^{J} p(M^{new} \mid Q^{new}, \underline{\theta}^j)}{J}$

This process can also be performed for repeated measurements of the same source, that is, where $\underline{M}^{new}$ is a vector, $\underline{M}^{new} = (M_1^{new}, \ldots, M_n^{new})$. Under the assumption that the uncertainty in each measurement is independent of previous measurements, conditional on Q^{new}, at step two, $p(\underline{M}^{new} \mid Q^{new}, \underline{\theta}^j) = \prod_{i=1}^{n} p(M_i^{new} \mid Q^{new}, \underline{\theta}^j)$.

The distribution $p(Q^{new})$ in Eq. (5) is the prior distribution of Q^{new}, where we assume the new measurement is independent of the controlled release data. This distribution can be informed using relevant pre-existing data, such as survey data on leak rates in the region where the measurement was made. This facilitates the natural synthesis of external data with controlled release data and the new observed measurement.

The posterior distribution of interest $p(Q^{new} \mid M^{new}, \underline{M})$ can be sampled as follows:

1. Draw a sample of size L from the prior distribution $p(Q^{new})$: $S = \{Q_1^{new}, \ldots, Q_L^{new}\}$
2. For $l = 1, \ldots, L$, approximate $p(M^{new} \mid Q_l^{new}, \underline{M})$ using the previously described algorithm
3. Calculate weights

$$w_l = \frac{p(M^{new} \mid Q_l^{new}, \underline{M})}{\sum_{k=1}^{L} p(M^{new} \mid Q_k^{new}, \underline{M})} \quad (7)$$

4. Resample from S with sampling probabilities w_l for $l = 1, \ldots, L$ to get a sample of size K from the posterior distribution $p(Q^{new} \mid M^{new}, \underline{M})$.

4.2.2. Set-up

The algorithm described in the previous section is demonstrated using the model selected in Sec. 4.1 for QOGI Operator C. We consider two data scenarios: one where a single measurement of a source is made, and one where five independent measurements of the same source are made. We also investigate two different prior distributions, $p(Q^{new})$, to show how information flows from the prior to the posterior distribution.

We simulate the process of performing measurements in the field (e.g., as part of a LDAR survey program) as follows: First, we choose a hypothetical true value for the source we will measure, which we set to $Q_i = 25$ kg/h. Then, we simulate "measurements" by drawing from the posterior predictive distribution defined in Sec. 3.1.2, $p(\tilde{M}_i \mid M_i, Q_i = 25 \text{ kg/hr})$. This is done five times to produce five independent "measurements" of the same source. Let $M_1^{new}, \ldots, M_5^{new}$ represent the five simulated measurement values: 20.3 kg/h, 11.7 kg/h, 8.9 kg/h, 16.2 kg/h, and 16.4 kg/h.

To understand how prior information impacts the estimates, we use two different prior distributions. The first prior is a uniform distribution where we only impose the upper limit of 200 kg/h, while the second is a log-normal distribution, as this distribution has been suggested to model leak rate distributions [42].

To summarise, we investigate four different scenarios:

1. Only M_1^{new} is used, and $p(Q^{new})$ is a uniform distribution from 0 to 200 kg/h.
2. All of $M_1^{new}, \ldots, M_5^{new}$ are used, and $p(Q^{new})$ is a uniform distribution from 0 to 200 kg/h.
3. Only M_1^{new} is used, and $p(Q^{new})$ is a log-normal distribution with shape parameter 1, location parameter equal to zero, and scale parameter equal to 2.6 [39]
4. All of $M_1^{new}, \ldots, M_5^{new}$ are used, and $p(Q^{new})$ is a log-normal distribution with shape parameter 1, location parameter equal to zero, and scale parameter equal to 2.6 [39]

4.2.3. Results

The different information expressed in the two priors can be visualized by comparing the histograms in Fig. 10. The uniform prior expresses that all values between 0 and 200 kg/h are equally likely. This may be a naive choice, because surveys have shown that extremely high emitters are much less likely than lower emitters [43, 42]. The log-normal prior expresses that there is about a 50% chance that the emission rate is less than 13.6 kg/h and 75% chance that the emission rate is less than 26.2 kg/h, with very large values being rare.

Also, posterior distributions are not centred around the measured values, which were all less than the "true" value of 25 kg/h. This is a reflection of the results shown in Fig. 5, where it is clear that the technology systematically underestimates the true emission rate. The algorithm presented in this section allows the information captured in the model derived from Sec. 3.1 to be inverted and produce estimates that are equal to the true emission rate, on average.

4.3. Discussion

As highlighted by Figs.3 - 9, relying solely on measurements without considering uncertainty can lead to significant misinterpretations of the emission rate. The methods presented in Sec 3.1 provide a way to summarise both the variability and systematic bias of a technology. They are situated in the Bayesian

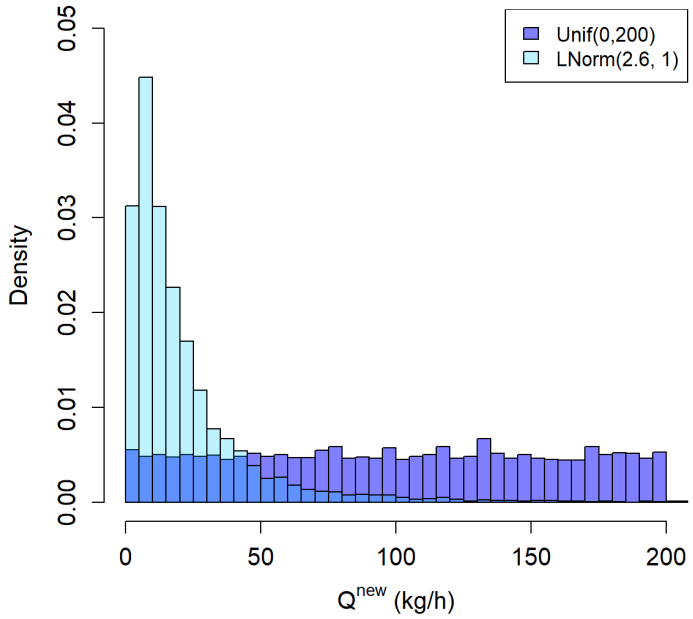

Figure 10: Comparison of histograms for the two different prior distributions $p(M^{new})$ investigated in the analysis.

statistical framework which facilitates probabilistic inference, the derivation of credible intervals, and downstream approaches, as exemplified in Sec. 4.2.

Specifically, the algorithm presented in Sec. 4.2 provides a distribution of the true emission rate given all available information, including a measurement or set of measurements, controlled release data, and external prior knowledge, e.g., what is a believable leak rate for a given scenario? This prior knowledge strongly informs the posterior when the measurement data is limited, but its influence diminishes as more measurements becomes available. This is beneficial because it formalises an informal process: in the absence of data, we must rely more on previous knowledge, whereas when more data are available, we rely less on our previous knowledge. The results also show that increasing the numbers of measurements reduces uncertainty in the posterior; that is, as we collect more data, we can be more certain about the true value of the emission rate. The models presented here could be used to determine how many measurements should be performed for a certain technology and emission rate to ensure that the credibility intervals are within a certain value. This algorithm in tandem with the models described in Sec. 3.1 could be used in the future to help plan or assess the effectiveness of LDAR programs, e.g., by identifying the optimal

Table 5: Summary of 90% credible intervals (CrI) for the four different data scenarios, and their lengths.

Prior	Number of Values	90% CrI	Length of CrI
Unif(0,200)	1	(12.3, 71.0)	58.7
Unif(0,200)	5	(14.9, 37.3)	22.3
LogNormal(2.6, 1)	1	(3.1, 47.9)	44.8
LogNormal(2.6, 1)	5	(13.9, 35.5)	21.6

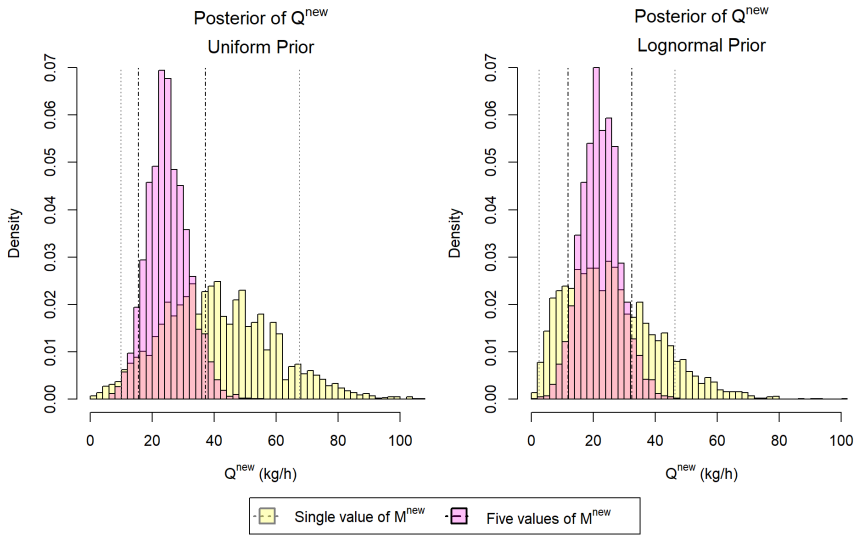

Figure 11: Posterior distributions for the true value of the emission rate given the observed measurement(s), prior distribution, and controlled release data.

combination of technologies that achieve a certain credibility interval.

Although extensive meteorological data were collected during the field trials (as detailed in the SI), we refrain from incorporating them in the statistical models. This is because the goal of the models is to summarise the performance of a technology over a variety of conditions. To this end, the field trials were conducted at different times-of-year and each trial over multiple days, so that the results could be used to assess the performance of the technologies over a variety of conditions. This also enabled the use of external validation - checking to see if data collected under one set of conditions can be used to predict data collected under a different set of conditions. However, it may be possible to improve the predictive performance of the models by incorporating meteorological data into the likelihood, discussed further in the Conclusion section.

5. Conclusions

A wide range of quantification technologies have been deployed to measure methane emissions from the upstream oil and gas sector, including ground-based infrared cameras, airborne hyperspectral imaging, and truck and airborne laser absorption spectroscopy. However, measurements from these technologies can only be interpreted properly in the context of uncertainty, which arise from measurement noise, uncertain model parameters, and, especially, the approximations and simplifications that must be made to render the models tractable (model error).

This paper presented a formalism for developing uncertainty estimates from controlled release data within the Bayesian framework. The outcome of this analysis are posterior probability density functions that comprehensively define what is known about an emission rate, based on the measurement data, controlled release data, and prior information. This approach is entirely technology-agnostic, does not require knowledge of the underlying physical model, and may be adapted to a wide range of scenarios.

The probability density functions may be summarized as credibility intervals (e.g., the range of emission rates that correspond to a given probability) and may be used for other purposes, such as the input to probabilistic simulations to assess the effectiveness of alternative fugitive emissions management plans (alt-FEMPS) or the in calculating the uncertainty attached to inventory estimates. This study demonstrates clearly the importance of multiple measurements during any particular emission survey study. Two implications of this result are immediately of significance for regulation and policy. Currently the structure and schedule of regulations tends to specify only the annual frequencies of site and equipment emission monitoring surveys (cite the Alberta or BC regulations if you wish). A key result of this study is that the uncertainty of a given survey is dependent on the number of measurements made. Due to the relatively large uncertainties observed for different technologies in this study, it is likely that multiple measurements would be required to achieve a desired emission rate uncertainty. Therefore, regulators would be advised to specify the minimum number of observations at any emission source in addition to the annual emissions survey frequencies. Alternatively, and perhaps more appropriately due to the relationship between uncertainty and true emission rate, a desired uncertainty range per emission source should be specified and the number of measurements required to achieve this uncertainty should be made.

An important aspect of methane detection and quantification technologies not covered by the methodology so far is the detection probability, that is, how likely it is that a technology will detect a given emission source under a set of conditions. Work has been done to characterise probability of detection and uncertainty separately, e.g., [22]. An advantage of the Bayesian approach taken in this paper is that it lends itself well to model extension. Modelling of detection probability could be done simultaneously to uncertainty modelling by using a hierarchical Bayesian model. Extending the model to simultaneously consider detection probability and measurement uncertainty is an important avenue of

future work.

Another area of further exploration lies in the incorporation of meteorological data into the likelihood. Given a large amount of controlled release data, it may be possible to narrow the posterior probability by incorporating the meteorological data into the likelihood. For example, the likelihood could be modified so that the median function is

$$\phi_i = \alpha_0 + \alpha_1 Q_i + \beta_1(\text{wind speed}_i).$$

In other words, the meteorological data becomes an additional observable. Another caveat to the inclusion of covariates is that more controlled release data would be needed to accurately estimate the increased number of model parameters. However, it has the potential to improve the predictive performance of the models. Incorporating meteorological data into the model could be investigated further.

6. Acknowledgements

This research was sponsored by the Alberta Upstream Petroleum Research Fund (AUPRF), the Clean Resources Information Network (CRIN), and the Natural Sciences and Engineering Research Council (ALLRP 571135-2021). The authors are grateful for the support of Carbon Management Canada, Petroleum Technology Alliance Canada, and Arolytics, Inc.

References

[1] K. Calvin, D. Dasgupta, G. Krinner, A. Mukherji, P. W. Thorne, C. Trisos, J. Romero, P. Aldunce, K. Barrett, G. Blanco, W. W. Cheung, S. Connors, F. Denton, A. Diongue-Niang, D. Dodman, M. Garschagen, O. Geden, B. Hayward, C. Jones, F. Jotzo, T. Krug, R. Lasco, Y.-Y. Lee, V. Masson-Delmotte, M. Meinshausen, K. Mintenbeck, A. Mokssit, F. E. Otto, M. Pathak, A. Pirani, E. Poloczanska, H.-O. Pörtner, A. Revi, D. C. Roberts, J. Roy, A. C. Ruane, J. Skea, P. R. Shukla, R. Slade, A. Slangen, Y. Sokona, A. A. Sörensson, M. Tignor, D. Van Vuuren, Y.-M. Wei, H. Winkler, P. Zhai, Z. Zommers, J.-C. Hourcade, F. X. Johnson, S. Pachauri, N. P. Simpson, C. Singh, A. Thomas, E. Totin, P. Arias, M. Bustamante, I. Elgizouli, G. Flato, M. Howden, C. Méndez-Vallejo, J. J. Pereira, R. Pichs-Madruga, S. K. Rose, Y. Saheb, R. Sánchez Rodríguez, D. Ürge Vorsatz, C. Xiao, N. Yassaa, A. Alegría, K. Armour, B. Bednar-Friedl, K. Blok, G. Cissé, F. Dentener, S. Eriksen, E. Fischer, G. Garner, C. Guivarch, M. Haasnoot, G. Hansen, M. Hauser, E. Hawkins, T. Hermans, R. Kopp, N. Leprince-Ringuet, J. Lewis, D. Ley, C. Ludden, L. Niamir, Z. Nicholls, S. Some, S. Szopa, B. Trewin, K.-I. Van Der Wijst, G. Winter, M. Witting, A. Birt, M. Ha, J. Romero, J. Kim, E. F. Haites, Y. Jung, R. Stavins, A. Birt, M. Ha, D. J. A. Orendain, L. Ignon, S. Park, Y. Park, A. Reisinger, D. Cammaramo, A. Fischlin, J. S. Fuglestvedt, G. Hansen,

C. Ludden, V. Masson-Delmotte, J. R. Matthews, K. Mintenbeck, A. Pirani, E. Poloczanska, N. Leprince-Ringuet, C. Péan, IPCC, 2023: Climate Change 2023: Synthesis Report. Contribution of Working Groups I, II and III to the Sixth Assessment Report of the Intergovernmental Panel on Climate Change [Core Writing Team, H. Lee and J. Romero (eds.)]. IPCC, Geneva, Switzerland., Tech. rep., Intergovernmental Panel on Climate Change (IPCC), edition: First (Jul. 2023). doi:10.59327/IPCC/AR6-9789291691647.
URL https://www.ipcc.ch/report/ar6/syr/

[2] A. Wilson, New Optical Gas-Imaging Technology for Quantifying Fugitive-Emission Rates, Journal of Petroleum Technology 68 (08) (2016) 78–79. doi:10.2118/0816-0078-JPT.
URL https://doi.org/10.2118/0816-0078-JPT

[3] A. L. Mitchell, D. S. Tkacik, J. R. Roscioli, S. C. Herndon, T. I. Yacovitch, D. M. Martinez, T. L. Vaughn, L. L. Williams, M. R. Sullivan, C. Floerchinger, M. Omara, R. Subramanian, D. Zimmerle, A. J. Marchese, A. L. Robinson, Measurements of Methane Emissions from Natural Gas Gathering Facilities and Processing Plants: Measurement Results, Environmental Science & Technology 49 (5) (2015) 3219–3227, publisher: American Chemical Society. doi:10.1021/es5052809.
URL https://doi.org/10.1021/es5052809

[4] R. Kang, P. Liatsis, D. C. Kyritsis, Emission Quantification via Passive Infrared Optical Gas Imaging: A Review, Energies 15 (9) (2022) 3304, number: 9 Publisher: Multidisciplinary Digital Publishing Institute. doi:10.3390/en15093304.
URL https://www.mdpi.com/1996-1073/15/9/3304

[5] R. S. Heltzel, D. R. Johnson, M. T. Zaki, A. K. Gebreslase, O. I. Abdul-Aziz, Machine learning techniques to increase the performance of indirect methane quantification from a single, stationary sensor, Heliyon 8 (12) (2022) e11962. doi:10.1016/j.heliyon.2022.e11962.
URL https://www.sciencedirect.com/science/article/pii/S2405844022032509

[6] H. L. Brantley, E. D. Thoma, W. C. Squier, B. B. Guven, D. Lyon, Assessment of Methane Emissions from Oil and Gas Production Pads using Mobile Measurements, Environmental Science & Technology 48 (24) (2014) 14508–14515, publisher: American Chemical Society. doi:10.1021/es503070q.
URL https://doi.org/10.1021/es503070q

[7] E. Atherton, D. Risk, C. Fougère, M. Lavoie, A. Marshall, J. Werring, J. P. Williams, C. Minions, Mobile measurement of methane emissions from natural gas developments in northeastern British Columbia, Canada, Atmospheric Chemistry and Physics 17 (20) (2017) 12405–12420, publisher:

Copernicus GmbH. doi:10.5194/acp-17-12405-2017.
URL https://acp.copernicus.org/articles/17/12405/2017/

[8] D. R. Caulton, Q. Li, E. Bou-Zeid, J. P. Fitts, L. M. Golston, D. Pan, J. Lu, H. M. Lane, B. Buchholz, X. Guo, J. McSpiritt, L. Wendt, M. A. Zondlo, Quantifying uncertainties from mobile-laboratory-derived emissions of well pads using inverse Gaussian methods, Atmospheric Chemistry and Physics 18 (20) (2018) 15145–15168, publisher: Copernicus GmbH. doi:10.5194/acp-18-15145-2018.
URL https://acp.copernicus.org/articles/18/15145/2018/

[9] B. M. Conrad, D. R. Tyner, H. Z. Li, D. Xie, M. R. Johnson, A measurement-based upstream oil and gas methane inventory for Alberta, Canada reveals higher emissions and different sources than official estimates, Communications Earth & Environment 4 (1) (2023) 1–10, number: 1 Publisher: Nature Publishing Group. doi:10.1038/s43247-023-01081-0.
URL https://www.nature.com/articles/s43247-023-01081-0

[10] E. D. Sherwin, Y. Chen, A. P. Ravikumar, A. R. Brandt, Single-blind test of airplane-based hyperspectral methane detection via controlled releases, Elementa: Science of the Anthropocene 9 (1) (2021) 00063. doi:10.1525/elementa.2021.00063.
URL https://doi.org/10.1525/elementa.2021.00063

[11] D. J. Varon, J. McKeever, D. Jervis, J. D. Maasakkers, S. Pandey, S. Houweling, I. Aben, T. Scarpelli, D. J. Jacob, Satellite Discovery of Anomalously Large Methane Point Sources From Oil/Gas Production, Geophysical Research Letters 46 (22) (2019) 13507–13516, _eprint: https://onlinelibrary.wiley.com/doi/pdf/10.1029/2019GL083798. doi:10.1029/2019GL083798.
URL https://onlinelibrary.wiley.com/doi/abs/10.1029/2019GL083798

[12] J. P. Canfin, Pascal, Report on the proposal for a regulation of the European Parliament and of the Council on methane emissions reduction in the energy sector and amending Regulation (EU) 2019/942 | A9-0162/2023 | European Parliament (Apr. 2023).
URL https://www.europarl.europa.eu/doceo/document/A-9-2023-0162_EN.html

[13] OGMP 2.0 – The Oil & Gas Methane Partnership 2.0.
URL https://ogmpartnership.com/

[14] T. A. Fox, C. H. Hugenholtz, T. E. Barchyn, T. R. Gough, M. Gao, M. Staples, Can new mobile technologies enable fugitive methane reductions from the oil and gas industry?, Environmental Research Letters 16 (6) (2021) 064077, publisher: IOP Publishing. doi:10.1088/1748-9326/ac0565.
URL https://dx.doi.org/10.1088/1748-9326/ac0565

[15] E. Solazzo, M. Crippa, D. Guizzardi, M. Muntean, M. Choulga, G. Janssens-Maenhout, Uncertainties in the Emissions Database for Global

Atmospheric Research (EDGAR) emission inventory of greenhouse gases, Atmospheric Chemistry and Physics 21 (7) (2021) 5655–5683, publisher: Copernicus GmbH. doi:10.5194/acp-21-5655-2021.
URL https://acp.copernicus.org/articles/21/5655/2021/

[16] K. MacKay, M. Lavoie, E. Bourlon, E. Atherton, E. O'Connell, J. Baillie, C. Fougère, D. Risk, Methane emissions from upstream oil and gas production in Canada are underestimated, Scientific Reports 11 (1) (2021) 8041, number: 1 Publisher: Nature Publishing Group. doi:10.1038/s41598-021-87610-3.
URL https://www.nature.com/articles/s41598-021-87610-3

[17] A. Montazeri, X. Zhou, J. D. Albertson, On the Viability of Video Imaging in Leak Rate Quantification: A Theoretical Error Analysis, Sensors 21 (17) (2021) 5683, number: 17 Publisher: Multidisciplinary Digital Publishing Institute. doi:10.3390/s21175683.
URL https://www.mdpi.com/1424-8220/21/17/5683

[18] M. O. L. Cambaliza, P. B. Shepson, D. R. Caulton, B. Stirm, D. Samarov, K. R. Gurney, J. Turnbull, K. J. Davis, A. Possolo, A. Karion, C. Sweeney, B. Moser, A. Hendricks, T. Lauvaux, K. Mays, J. Whetstone, J. Huang, I. Razlivanov, N. L. Miles, S. J. Richardson, Assessment of uncertainties of an aircraft-based mass balance approach for quantifying urban greenhouse gas emissions, Atmospheric Chemistry and Physics 14 (17) (2014) 9029–9050, publisher: Copernicus GmbH. doi:10.5194/acp-14-9029-2014.
URL https://acp.copernicus.org/articles/14/9029/2014/

[19] D. Singh, B. Barlow, C. Hugenholtz, W. Funk, C. Robinson, A. P. Ravikumar, Field Performance of New Methane Detection Technologies: Results from the Alberta Methane Field Challenge, publisher: EarthArXiv (Jun. 2021).
URL https://eartharxiv.org/repository/view/1860/

[20] M. R. Johnson, D. R. Tyner, A. J. Szekeres, Blinded evaluation of airborne methane source detection using Bridger Photonics LiDAR, Remote Sensing of Environment 259 (2021) 112418. doi:10.1016/j.rse.2021.112418.
URL https://www.sciencedirect.com/science/article/pii/S003442572100136X

[21] C. Bell, J. Rutherford, A. Brandt, E. Sherwin, T. Vaughn, D. Zimmerle, Single-blind determination of methane detection limits and quantification accuracy using aircraft-based LiDAR, Elementa: Science of the Anthropocene 10 (1) (2022) 00080. doi:10.1525/elementa.2022.00080.
URL https://doi.org/10.1525/elementa.2022.00080

[22] B. M. Conrad, D. R. Tyner, M. R. Johnson, Robust probabilities of detection and quantification uncertainty for aerial methane detection: Examples for three airborne technologies, Remote Sensing of Environment 288 (2023) 113499. doi:10.1016/j.rse.2023.113499.
URL https://www.sciencedirect.com/science/article/pii/S0034425723000500

[23] C. E. Kemp, A. P. Ravikumar, A. R. Brandt, Comparing Natural Gas Leakage Detection Technologies Using an Open-Source "Virtual Gas Field" Simulator, Environmental Science & Technology 50 (8) (2016) 4546–4553, publisher: American Chemical Society. doi:10.1021/acs.est.5b06068.
URL https://doi.org/10.1021/acs.est.5b06068

[24] T. A. Fox, M. Gao, T. E. Barchyn, Y. L. Jamin, C. H. Hugenholtz, An agent-based model for estimating emissions reduction equivalence among leak detection and repair programs, Journal of Cleaner Production 282 (2021) 125237. doi:10.1016/j.jclepro.2020.125237.
URL https://www.sciencedirect.com/science/article/pii/S0959652620352811

[25] M. Lavoie, D. Risk, E. O'Connell, E. Atherton, J. Gorski, J. Johnson, Evaluating the benefits of alternative leak detection programs, publisher: EarthArXiv (May 2021).
URL https://eartharxiv.org/repository/view/2355/

[26] M. R. Johnson, B. M. Conrad, D. R. Tyner, Creating measurement-based oil and gas sector methane inventories using source-resolved aerial surveys, Communications Earth & Environment 4 (1) (2023) 1–9, number: 1 Publisher: Nature Publishing Group. doi:10.1038/s43247-023-00769-7.
URL https://www.nature.com/articles/s43247-023-00769-7

[27] Y. Zeng, J. Morris, Detection limits of optical gas imagers as a function of temperature differential and distance, Journal of the Air & Waste Management Association 69 (3) (2019) 351–361, publisher: Taylor & Francis _eprint: https://doi.org/10.1080/10962247.2018.1540366. doi:10.1080/10962247.2018.1540366.
URL https://doi.org/10.1080/10962247.2018.1540366

[28] A. P. Ravikumar, J. Wang, M. McGuire, C. S. Bell, D. Zimmerle, A. R. Brandt, "Good versus Good Enough?" Empirical Tests of Methane Leak Detection Sensitivity of a Commercial Infrared Camera, Environmental Science & Technology 52 (4) (2018) 2368–2374, publisher: American Chemical Society. doi:10.1021/acs.est.7b04945.
URL https://doi.org/10.1021/acs.est.7b04945

[29] D. Zimmerle, T. Vaughn, C. Bell, K. Bennett, P. Deshmukh, E. Thoma, Detection Limits of Optical Gas Imaging for Natural Gas Leak Detection in Realistic Controlled Conditions, Environmental Science & Technology 54 (18) (2020) 11506–11514, publisher: American Chemical Society. doi:10.1021/acs.est.0c01285.
URL https://doi.org/10.1021/acs.est.0c01285

[30] J. M. Supplee, E. A. Whittaker, W. Lenth, Theoretical description of frequency modulation and wavelength modulation spectroscopy, Applied Optics 33 (27) (1994) 6294–6302, publisher: Optica Publishing Group. doi:10.1364/AO.33.006294.
URL https://opg.optica.org/ao/abstract.cfm?uri=ao-33-27-6294

[31] T. K. Flesch, J. D. Wilson, E. Yee, Backward-Time Lagrangian Stochastic Dispersion Models and Their Application to Estimate Gaseous Emissions, Journal of Applied Meteorology and Climatology 34 (6) (1995) 1320–1332, publisher: American Meteorological Society Section: Journal of Applied Meteorology and Climatology. doi:10.1175/1520-0450(1995)034¡1320:BTLSDM¿2.0.CO;2.
URL https://journals.ametsoc.org/view/journals/apme/34/6/1520-0450_1995_034_1320_btlsdm_2

[32] T. K. Flesch, J. D. Wilson, L. A. Harper, B. P. Crenna, R. R. Sharpe, Deducing Ground-to-Air Emissions from Observed Trace Gas Concentrations: A Field Trial, Journal of Applied Meteorology and Climatology 43 (3) (2004) 487–502, publisher: American Meteorological Society Section: Journal of Applied Meteorology and Climatology. doi:10.1175/1520-0450(2004)043¡0487:DGEFOT¿2.0.CO;2.
URL https://journals.ametsoc.org/view/journals/apme/43/3/1520-0450_2004_043_0487_dgefot_2

[33] A. E. Esparza, J.-F. Gauthier, Monitoring Leaks at Oil and Gas Facilities Using the Same Sensor on Aircraft and Satellite Platforms, OnePetro, 2021. doi:10.15530/urtec-2021-5666.
URL https://dx.doi.org/10.15530/urtec-2021-5666

[34] A. E. Esparza, G. Rowan, A. Newhook, H. J. Deglint, B. Garrison, B. Orth-Lashley, M. Girard, W. Shaw, Analysis of a tiered top-down approach using satellite and aircraft platforms to monitor oil and gas facilities in the Permian basin, Renewable and Sustainable Energy Reviews 178 (2023) 113265. doi:10.1016/j.rser.2023.113265.
URL https://www.sciencedirect.com/science/article/pii/S1364032123001211

[35] D. J. Varon, D. J. Jacob, J. McKeever, D. Jervis, B. O. A. Durak, Y. Xia, Y. Huang, Quantifying methane point sources from fine-scale satellite observations of atmospheric methane plumes, Atmospheric Measurement Techniques 11 (10) (2018) 5673–5686, publisher: Copernicus GmbH. doi:10.5194/amt-11-5673-2018.
URL https://amt.copernicus.org/articles/11/5673/2018/

[36] A. Gelman, J. B. Carlin, H. S. Stern, D. B. Dunson, A. Vehtari, D. B. Rubin, Bayesian Data Analysis, Third Edition, CRC Press, 2013, google-Books-ID: ZXL6AQAAQBAJ.

[37] M. Plummer, JAGS version 4.3.0 user manual (Jun. 2023).
URL http://www.stat.yale.edu/ jtc5/238/materials/jags_4.3.0_manual_with_distributions.pd

[38] M. J. Denwood, runjags: An R Package Providing Interface Utilities, Model Templates, Parallel Computing Methods and Additional Distributions for MCMC Models in JAGS, Journal of Statistical Software 71 (2016) 1–25. doi:10.18637/jss.v071.i09.
URL https://doi.org/10.18637/jss.v071.i09

[39] NIST, 1.3.6.6.9. Lognormal Distribution (Jun. 2023).
URL https://www.itl.nist.gov/div898/handbook/eda/section3/eda3669.htm

[40] A. Gelman, Prior distributions for variance parameters in hierarchical models (comment on article by Browne and Draper), Bayesian Analysis 1 (3) (2006) 515–534, publisher: International Society for Bayesian Analysis. doi:10.1214/06-BA117A.
URL https://projecteuclid.org/journals/bayesian-analysis/volume-1/issue-3/Prior-distrib

[41] D. J. Spiegelhalter, N. G. Best, B. P. Carlin, A. Van Der Linde, Bayesian measures of model complexity and fit, J R Stat Soc Series B Stat Methodology 64 (4) (2002) 583–639.

[42] D. Zavala-Araiza, S. C. Herndon, J. R. Roscioli, T. I. Yacovitch, M. R. Johnson, D. R. Tyner, M. Omara, B. Knighton, Methane emissions from oil and gas production sites in Alberta, Canada, Elementa: Science of the Anthropocene 6 (2018) 27. doi:10.1525/elementa.284.
URL https://doi.org/10.1525/elementa.284

[43] A. R. Brandt, G. A. Heath, D. Cooley, Methane Leaks from Natural Gas Systems Follow Extreme Distributions, Environmental Science & Technology 50 (22) (2016) 12512–12520, publisher: American Chemical Society. doi:10.1021/acs.est.6b04303.
URL https://doi.org/10.1021/acs.est.6b04303